




Method for nanoparticles uptake evaluation based on double labeled fluorescent cells scanned in enhanced darkfield microscopy

MONA MIHAILESCU,^{1,2} LUMINITA C. MICLEA,^{3,7,†} ANA M. PLEAVA,^{4,8,†} NICOLAE TARBA,⁵ EUGEN N. SCARLAT,¹ RALUCA D. NEGOITA,⁶ MIHAELA G. MOISESCU,³  AND TUDOR SAVOPOL³ 

¹Holographic Imaging and Processing Laboratory, Physics Department, Politehnica University Bucharest, 313 Splaiul Independentei, Bucharest, 060042, Romania

²Centre for Research in Fundamental Sciences Applied in Engineering, Politehnica University Bucharest, 313 Splaiul Independentei, Bucharest, 060042, Romania

³Department of Biophysics and Cellular Biotechnology, Research Center of Excellence in Biophysics and Cellular Biotechnology, Faculty of Medicine, Carol Davila University of Medicine and Pharmacy, 8 Eroii Sanitari Blvd., 050474 Bucharest, Romania

⁴CAMPUS Research Center, University "Politehnica" of Bucharest, 313 Splaiul Independentei, Bucharest, 060042, Romania

⁵Doctoral School of Automatic Control and Computers, Physics Department, Faculty of Applied Sciences, University "Politehnica" of Bucharest, 313 Splaiul Independentei, Bucharest, 060042, Romania

⁶Applied Sciences Doctoral School, Politehnica University of Bucharest, 313 Splaiul Independentei, Bucharest, 060042, Romania

⁷luminita.miclea@umfcd.ro

⁸ana_maria.sandu@upb.ro

[†]These authors contributed equally

Abstract: We present a method that integrates the standard imaging tools for locating and detecting unlabeled nanoparticles (NPs) with computational tools for partitioning cell volumes and NPs counting within specified regions to evaluate their internal traffic. The method uses enhanced dark field CytoViva optical system and combines 3D reconstructions of double fluorescently labeled cells with hyperspectral images. The method allows the partitioning of each cell image into four regions: nucleus, cytoplasm, and two neighboring shells, as well as investigations across thin layers adjacent to the plasma membrane. MATLAB scripts were developed to process the images and to localize NPs in each region. Specific parameters were computed to assess the uptake efficiency: regional densities of NPs, flow densities, relative accumulation indices, and uptake ratios. The results of the method are in line with biochemical analyses. It was shown that a sort of saturation limit for intracellular NPs density is reached at high extracellular NPs concentrations. Higher NPs densities were found in the proximity of the plasma membranes. A decrease of the cell viability with increasing extracellular NPs concentration was observed and explained the negative correlation of the cell eccentricity with NPs number.

© 2023 Optica Publishing Group under the terms of the [Optica Open Access Publishing Agreement](#)

1. Introduction

Based on an increasingly need to better understand of the nanoparticles (NPs) effects on living cells [1], their use in biology and medicine has grown considerably in recent years.

A key point for a deeper knowledge of NPs effects on living cells is to properly track their pathway from membrane penetration to their final destination [2,3]. Diverse NPs parameters like chemical structure, shape, size, area, surface charge, as well as on the cell type [3] determine their intracellular fate.

Considered as “the third most commonly used metal-containing nanomaterial” [4], the engineered zinc oxide nanoparticles (ZnO-NPs) are used for various purposes [5–9]. It is thus of interest to study the *in vivo* and *in vitro* effects of their interactions with human or animal organisms down to the cellular level.

Conventional imaging methods used to detect NPs inside cells are electron microscopy - mainly for NPs in biopsy tissues [10], atomic force microscopy - to study the NPs impact on cells biophysical properties [11–13], or scanning transmission X-ray microscopy - for tomographic reconstructions [14,15]. These techniques have high resolution, but small field of view. Besides, they are expensive and cumbersome in terms of sample preparation.

On the other side, the optical microscopy offers larger fields of view, allowing to visualize living cells in their culture medium, in real-time, with the drawback of low resolution. Fluorescence microscopy uses labeled NPs and cells to detect NPs uptake and time-based acquisitions to track NPs within the cells [16]. Confocal microscopy is a technique allowing to qualitatively determine if labeled nanoparticles are inside or outside the cell [17]. Super-resolution microscopy pushes the resolution limit down to 50 nm [18], being able to identify nanoparticles features well below the diffraction limit [19]. Enhanced dark field microscopy (eDFM) proved to be a promising tool to visualize NPs in cells (either labeled or not). eDFM detects the Rayleigh scattering of the incident light by nanometric scale objects (e.g., NPs located intra- or extra-cellularly). The intensity of the scattered light is dependent on the size, chemical composition and refractive index of the NPs [20,21]. The method has been previously used to investigate cells dynamic [22], Au or Ag NPs [23,24].

eDFM can be effectively improved when combined with hyperspectral microscopy (HSM), which helps to detect NPs' scattering spectra [25–27]. The NPs presence is established by identifying the characteristic scattering properties and the relevant spectral profiles of each NPs type, at pixel level. This combination of techniques was initially developed for metallic NPs using their plasmon resonance properties [28–30] and later used also for non-metallic NPs [31–33]. eDFM can also be improved by combining it with fluorescence microscopy. Using a Z-scan technique under eDFM examination mode in a CytoViva-adapted system including a fluorescent module, it is possible to visualize 3D distribution of NPs inside structured substrates [34,35], 3D reconstruction of cells and the intracellular NPs distribution [36], or to study fluorescently labeled organelles [37]. Therefore, a less interfering and more accessible method for visualizing and localizing NPs within living cells is of high interest, especially if they do not require labeled NPs. Many laboratories reported automated methods and strategies to process fluorescence [38], hyperspectral [39], darkfield [40] images or developed computational models [41] to evaluate cellular uptake potential.

In the present work we exploit the advantages provided by combining the CytoViva facilities, i.e., eDFM, HSM and fluorescence microscopy, to develop numerical tools to quantitatively assess the uptake efficiency of unlabeled NPs within cells. The method consists of scripts devoted to precise localization and counting of NPs in the cytoplasm, nucleus, and border areas, thus enabling the computation of geometric parameters of the cells (perimeters, areas, eccentricity, volumes). The method furnishes output parameters to characterize intracellular processes like particle densities per region and per the whole cell, gradients, NPs distribution along the cell height, uptake ratios, flow density through lateral area, correlation coefficients, relative accumulation indices. These scripts were tested on images from Z-scan of fluorescently double-labeled NIH3T3 cells incubated with ZnO-NPs. Characteristic spectral profiles of ZnO-NPs were identified using HSM images.

2. Samples preparation and images acquisition

2.1. Samples preparation

ZnO-NPs were synthesized through co-precipitation as described in [42]. ZnO-NPs were sterilized at 121. °C in dry atmosphere and stock sterile suspensions of 2000.µg/ml were prepared in phosphate buffered saline solution (PBS) (NaCl 146.mM, KCl 2.6.mM, Na₂HPO₄ 10.14.mM, KH₂PO₄ 1.76 mM, pH 7.4), then sonicated on ice for 45 minutes and diluted in complete culture medium at working concentrations of 1, 2, 3, 4, 8, 16 and 32 µg/mL.

Murine embryonic fibroblast cell line NIH3T3 (ATCC-CRL 1658) was used. Cells were grown in Dulbecco's Modified Eagle Medium containing glucose (4.5 g/L), L-glutamine (2 mM) (DMEM) (Sigma-Aldrich, D5796, USA), supplemented with 10% Fetal Bovine Serum (Sigma-Aldrich, F7524, USA).

For microscopy experiments, cells were seeded on round glass coverslips (12 mm diameter), placed in a 24-wells culture plate (Corning Costar, CLS3527, EU) at a concentration of 4000 cells/well and let to grow for 24 h to resume the cell cycle. The culture medium from each well of the plate was then replaced with the NPs suspensions at working concentrations and cells were further incubated for 24 h. Afterward, the NPs suspensions were removed and the cells were washed with PBS and then fixed. For examination in CytoViva Z-scan fluorescence module, the samples were stained for cytoplasm with Alexa Fluor 488 Phalloidin (Alexa488, Invitrogen, ThermoFischer Scientific, A12379, USA) and for nucleus with 4',6-diamidino-2-phenylindole (DAPI, Sigma-Aldrich, D9542, EU), and mounted as previously described [36]. Three identical samples were prepared for the following working concentrations of NPs: 1, 2, 3, 8, and 32 µg/mL.

For cell viability experiments, cells were seeded (4000cells/well) in 96 well plates (TPP, 93040, Switzerland) and let to grow for 24 h (37 °C, humidified 5% CO₂ atmosphere). The incubation of cells with ZnO-NPs followed the same procedure as described above. The standard metabolic viability test (CellTiter 96 Aqueous One Solution Cell Proliferation Assay kit, Promega, G3581, USA) was used. The test is based on the reduction of a tetrazolium compound [3-(4,5-dimethylthiazol-2-yl)-5-(3-carboxymethoxyphenyl)-2-(4-sulphophenyl)-2H-tetrazolium, inner salt; MTS] by viable cells to generate the colored formazan dye that is soluble in cell culture media. The formazan concentration, which can be determined by measuring the optical density of the solution at 490 nm, is thus directly proportional to the number of metabolically viable cells within the sample [43]. All measurements were done in triplicates and data were normalized to the average value of the control (samples without NPs).

2.2. Hyperspectral imaging

To obtain hyperspectral images (HSI) of high resolution, CytoViva eDFM hyperspectral module (Fig. 1(a)) uses a white light source (FiberLite DC-950, 150 W quartz halogen aluminum reflector, Dolan Jenner Industries, USA) which illuminates the sample at a high oblique angle through a cardioid-shaped, oil immersed darkfield condenser, via an optical fiber with a liquid core. This particular setup improves the signal-to-noise ratio. The result consists in two-dimensional images with bright zones on a very dark background. The nanometric components of the sample scatter the incident light and send it through a 60× oil immersed objective to a spectrophotometer (ImSpectrum V10E, Specim Finland) which is equipped with a transmission diffraction grating inserted between the objective and a hyperspectral camera (Pixelfly 1392 × 1040-pixel resolution, 6.45 × 6.45 µm pixel size, 7.3 to 13.5 fps, 5 µs-60 s exposure time range, 62% quantum efficiency). The system provides a complete scattering spectrum at single pixel level in the range of 400-1000 nm with 1.28 nm spectral resolution. During image acquisition, the samples are scanned in the XY plane with a motorized stage (NanoScanZ, Prior Scientific Instruments Ltd, UK, 10 nm step size, 114 × 75 mm travel range). HSI were recorded and processed under Environment for Visualizing Images (ENVI) software [44,45]. The specific settings used for HSI acquisition were:

0.80 NA for 60x microscope objective, and 0.25 s exposure time for each scanned line (500 lines per each image).

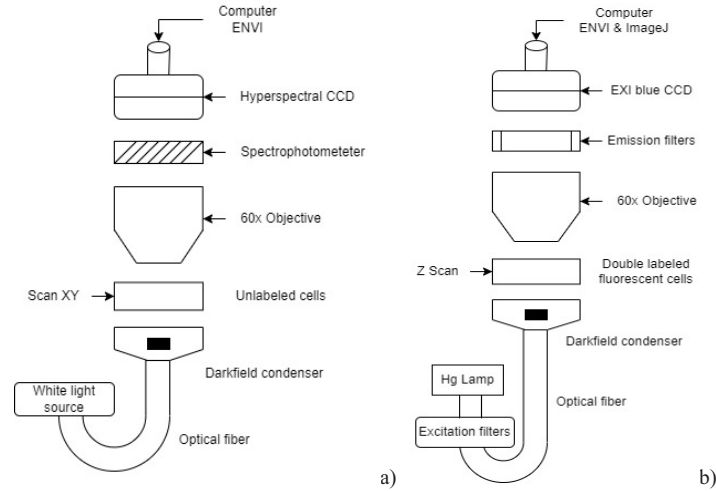


Fig. 1. Principal components of the experimental configurations a) hyperspectral and b) 3D fluorescent modules.

2.3. Z-scan of the double labeled fluorescent cells

To obtain a 3D map of relevant cell regions and of the whole cell, a new experimental step was added. It enhances the functionality of Z-scan and fluorescence modules mounted on the eDFM CytoViva system (Fig. 1(b)) and consists in imaging the samples labeled with two fluorophores (as described in Chp.2.1). Accordingly, two sets of images could be recorded consecutively, by Z-scan of the cells along their height (OZ axis) via two excitation filters inserted in the optical path: F1 for DAPI, and F2 for AlexaFluor488. To visualize the fluorescent images, an additional filter F4 allowed to record images simultaneously with both markers. A mercury lamp (Lumen200, Prior Scientific Instruments Ltd, UK) illuminates the darkfield condenser (the same as in the case of HSM), through a liquid optical fiber to diminish thermal noise. The images are formed on a cooled EXiBlue monochrome CCD (QIMAGING Corporation, Canada, 1392×1040 pixels, 15 fps at maximum resolution, $6.45 \times 6.45 \mu\text{m}$ pixel size). When the F4 filter is inserted, images in real fluorescent colors are acquired using OCULAR software and color QIMAGING CCD ($4.54 \times 4.54 \mu\text{m}$ pixel size, 75% quantum efficiency, Sony sensor 2688×2200 pixels, 7.1 fps).

In Figs. 1(a), (b) are shown the experimental configurations for hyperspectral and 3D fluorescent modules. They are integrated on the same microscope, but with some differences: the light source, the scanning mode, the type of sample analyzed, the detection device, and the preprocessing software.

Using the F1 filter and an oil immersed 60x objective (1.25 NA, 1 pixel in the XY plane corresponds to 107.5 nm), the nucleus was visualized as a set of N cross-sections (NZ), 100 nm apart ($\Delta z = 100 \text{ nm}$), grouped in F1-Z-stack images. Using the F2 filter, the images for cytoplasm were acquired as a set of F2-Z-stack images with the same number NZ of cross-sections (Fig. 2), the same focusing distance (no mechanical movements) and the same Δz .

Finally, ZnO-NPs presence was evidenced by illuminating the sample in “white” mercury light (WL) and a WL-Z-stack of scattered light images was acquired (NZ, Δz and focusing position remaining unchanged).

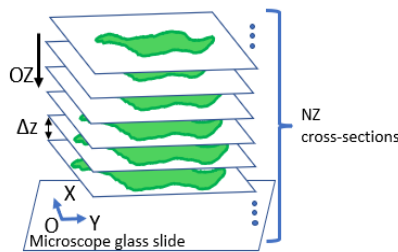


Fig. 2. Scheme of Z-stacks images acquisition, $\Delta z = 100$ nm, $NZ \cong 60$.

The exposure time was set as follows: 1000 ms for F1-Z-stacks, and between 600-800 ms for F2-Z-stacks (to avoid CCD saturation). In “white” mercury light, the exposure time was set under 50 ms to record only the intensity scattered by the nanoparticles and not the one coming from the cell which remains below the detecting threshold.

For F1-Z- and F2-Z-stacks, the point spread function and deconvolution routines provided by the CytoViva producer were run while for WL-Z-stacks, the built-in specific plugin “Just locate nanoparticles” was used [46].

3. Method description

3.1. Hyperspectral analysis

The hyperspectral investigation is necessary to prove the existence of ZnO-NPs inside the cells. The presence of ZnO-NPs further justifies the 3D quantitative analysis of the sample. HSI were acquired on two categories of samples: samples consisting of ZnO-NPs in culture medium, and samples consisting of cells incubated with ZnO-NPs in different extracellular concentrations. The spectral fingerprints of ZnO-NPs inside cells were saved in spectral library and further used to identify the ZnO-NPs inside cells in all samples by running the built-in spectral angle mapper (SAM) under ENVI software. The spectrum from each pixel was compared to the fingerprint stored in the spectral library, and, if they had similar shapes, the pixels were turned in red color.

3.2. Cells regions and ZnO-NPs distribution

To evaluate the 3D distribution of ZnO-NPs per region and per whole cell, we introduced specific MATLAB scripts (R2022a MathWorks, USA). They rely on the “slicing” procedure provided by Z-scan module and allow NPs counting in each region as well in the whole cell by summing the counted values from all slices. Our scripts identify the edges of the nucleus and cytoplasm in each cross-section of F1-Z-stack and F2-Z-stack, respectively. During image acquisition, the exposure time was set to avoid the CCD saturation, therefore some pixels might darken after deconvolution and consequently, the fluorescence images might exhibit “cavities” and open contours. The challenge was to find a unique rule to automatically generate continuous and realistic contours that fit the actual images of cells and to further allow the computation of the geometric parameters and NPs densities. Two approaches were tested: convex hull [47] and alpha shape [48].

In Fig. 3(top row), three examples of experimental fluorescence images are given (one cross-section per each F2-Z-stack). Figure 3(bottom row) displays the deconvolved images (white shapes) interpolated according to convex hull (red) and alpha shape approach (blue). One can easily remark that the blue interpolations are better filling the gap areas between the white shapes and thus providing continuous contours, closer to experimental images. For a given cross-section, the parameter alpha value (α) was chosen empirically as the minimum value which leads to a cell shape with all points connected (the algorithm obeying the same rules for all

cross-sections). When computing the geometrical parameters, the entire area inside the blue contour was considered.

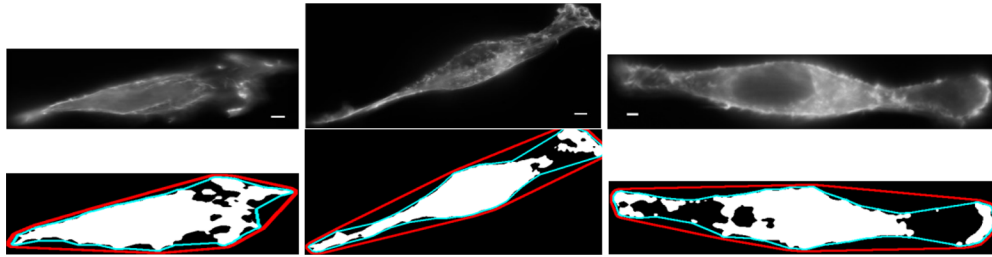


Fig. 3. Upper row: examples of three experimental fluorescence images (cross-sections from three different F2-Z-stacks). Bottom row: results of the deconvolution of corresponding F2-Z-stack fluorescence images (white) and of the filling procedures convex hull (red contour) and alpha shape (blue contour). The scale bars represent 2 μm .

To compute the NPs intracellular densities, a home-made MATLAB script was developed to partition the cell image into four relevant regions (Fig. 4): nucleus, shell 1 (a border region surrounding the nucleus), cytoplasm and shell 2 (a border region, inside the cytoplasm, adjacent to the plasma membrane). The rationale of defining shell 1 and shell 2 was for a deeper insight on the biochemical discontinuities that occur between cytoplasm- nucleus on one side, and between cytoplasm-extracellular medium on the other. Our method provides more detailed quantitative information on the particle density in each region which might help to better explain the trafficking mechanisms (in good agreement with reports in [2,3,14]).

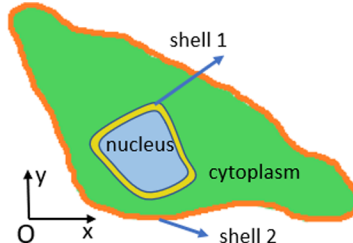


Fig. 4. Scheme of cellular regions: nucleus, shell 1, cytoplasm, shell 2.

In our test example, the same value was chosen for the widths of the shells (12 pixels $\sim 1.3 \mu\text{m}$). The choice was in line with experimental evidences of higher intensities in such regions, in both fluorescence and hyperspectral images. The MATLAB script was run on the filled images resulted from F1- and F2-Z-stacks. The script assigns the positions of ZnO-NPs to one of the four cellular regions according to their (X, Y, Z) coordinates stored in WL-Z-stack.

3.3. Parameters related to uptake efficiency

The MATLAB scripts also deliver a registry containing: i/ cell geometric parameters (the volumes of each region and of the whole cell, cell lateral area, eccentricity), and ii/ the number of ZnO-NPs per region. The volume of each region is computed by summing the products of each cross-section area by the distance between cross sections ($\Delta z = 100 \text{ nm}$). The lateral area of each cell is computed by summing the cell perimeters calculated in each cross-section multiplied by the axial step Δz . Cell eccentricity is computed using MATLAB eccentricity function on the cell cross-section with the maximum area among all images from a given F2-Z-stack.

The geometric parameters allow to compute a list of output parameters for each cell: i/ particle density per region and per the whole cell (as the ratio between the number of ZnO-NPs and volume of the region/cell), ii/ gradients of particle density g_1 , g_2 , and g_3 (we considered four layers of 650 nm width each, starting from the cell membrane towards the cell interior and the standard definition of discrete gradients was used), iii/ axial distribution of ZnO-NPs along the Z axis (particle densities computed by grouping the NZ cross-sections from a Z-stack into 6 equal intervals, and normalize their values to maximum value from all groups), iv/ uptake ratio (ratio between the particle density in the whole cell and extracellular concentration of ZnO-NPs in the culture medium), v/ flow density (number of particles entering the cell per 24.h, divided by the lateral area of the cell), vi/ correlation coefficients (between geometric parameters and number of NPs inside cell), vii/ relative accumulation index (RAI, as the ratio of the actual number of ZnO-NPs within each region to the expected number of NPs, computed under the null hypothesis of uniform distribution of ZnO-NPs inside cell for a specified extracellular concentration). The output parameters were computed as mean values for 15 cells for each extracellular ZnO-NPs concentration.

The Matlab script, on average, needs approximately 30 - 40 s and 30 MB of memory per image to compute all geometrical parameters and to list the output parameters on an Intel i5 9600 K processor. If, additionally, each image is saved on SSD, the average processing time per image rises to 45 s but the memory usage remains unchanged.

ANOVA tests (F-test and p-value) were used to investigate if the means ZnO-NPs densities across the four regions were statistically different (in the null hypothesis of uniform distribution) [49]: i/ comparison between the observed value of F and the critical value (F_{crit}), ii/ calculation of the probability p-value and comparing it with significance level.

Because the producer describes the 3D visualization procedure when only one fluorescent Z-stack and one WL-Z-stack are recorded [46], we propose a procedure (under ImageJ plugins) to visualize the 3D reconstruction of the cell with NPs, where all three Z-stacks (F2-Z-, F1-Z- and WL-Z-) were combined. The F2-Z-, F1-Z- and WL-Z-stacks were loaded (in this order) as “Surface” in the special plugin “3D viewer” of ImageJ. Then, the “Transparency” function was applied and adjusted until one could see “through” the cytoplasm or nucleus by keeping the genuine edges unaffected.

4. Results and discussions

The usefulness of the method is exemplified in the results below. They were obtained by performing hyperspectral identification of ZnO-NPs and by running MATLAB scripts for cell mapping, computation of geometrical and output parameters listed above.

4.1. Hyperspectral identification of ZnO-NPs in cells

The spectral profile of ZnO-NPs in culture medium (Fig. 5(blue curve)) showed bell-shaped curve with maximum in the range 477-485 nm, due to the slightly different size of the nanoparticles. The presence of the ZnO-NPs inside cells leads to pixels with intensity several orders of magnitude higher than the intensity scattered by the cellular structures. The spectral fingerprints of ZnO-NPs inside cells (Fig. 5(red curve)) detected in these pixels exhibit shifted maxima centered in the range 521-545 nm.

The fingerprints were stored as specimens in the “spectral library”. Differences between the spectral profiles of the nanoparticles outside and inside the cell (as well as different optical responses of the particles in different compartments inside the cells), have already been reported in the literature [26,50,51]. These differences may be explained by intricate mechanisms inside the cell where macromolecules adhere to NPs and change not only their chemical identity, but

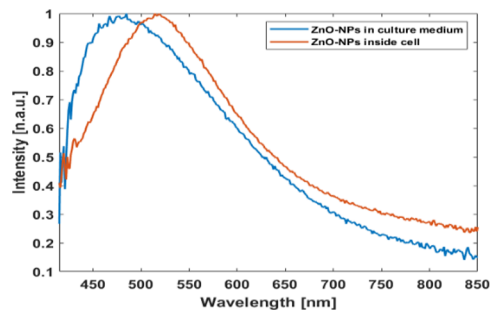


Fig. 5. Typical ZnO-NPs scattered spectra in culture medium (blue curve) and inside cell (red curve).

also their clustering properties. Next, NPs presence was investigated in all cellular samples for all working extracellular concentrations of ZnO-NPs.

In Fig. 6, the hyperspectral images of a cell incubated with ZnO-NPs (a) the appropriate identification of ZnO-NPs using SAM protocol (b) and their superposition (c) are shown.

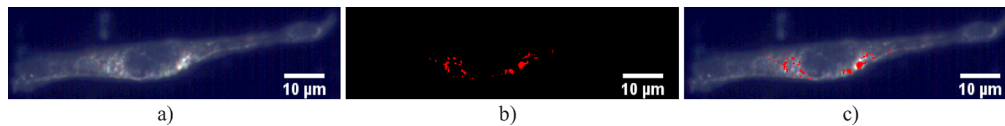


Fig. 6. a) Hyperspectral image of cell incubated with ZnO-NPs at 8 µg/mL extracellular concentration, b) identified ZnO-NPs (as red dots) according to SAM procedure, c) superposed images a) and b). The experimental image a), obtained by a single scan (line by line) of the sample, contains in each pixel the entire spectrum 400-1000 nm.

Two types of distribution within cells can be observed: ZnO-NPs either accumulate near the cell membrane (Fig. 7(a)), or spread inside the cell (Fig. 7(b)); these findings are confirmed by 3D analyses presented further.

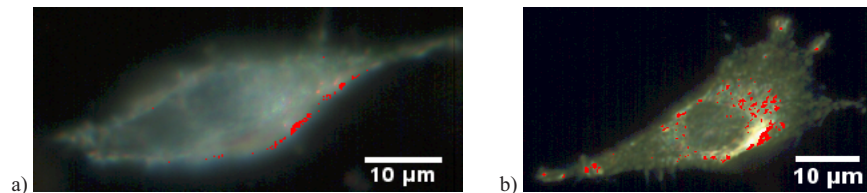


Fig. 7. Hyperspectral images of a) ZnO-NPs accumulated near the cell membrane for extracellular concentration of 1 µg/mL, b) ZnO-NPs spread inside the cell for extracellular concentration of 8 µg/mL. The experimental image a), obtained by a single scan (line by line) of the sample, contains in each pixel the entire spectrum 400-1000 nm.

4.2. 3D cell regions by Z-stacks

Figure 8(a) exemplifies a fluorescence image of a cell group acquired through F4 filter on the color QImaging CCD. Examples of experimental cross-sections from F1- and F2-Z-stacks are represented in Figs. 8(b) and (c), respectively (acquired using monochrome QIMAGING CCD). The corresponding images after deconvolution (obtained using the built-in CytoViva routine) are given in Figs. 8(d), e. Running the routine “Just locate nanoparticles” on WL-Z-stacks, the

nanoparticles were identified and their coordinates stored as triplets: X , Y , and the cross-section index Z ; the size and color of the points representing NPs were chosen by the user (red in Fig. 8(f)). 3D reconstructions of cells incubated with NPs were done under ImageJ using our procedure (Figs. 8(g)-(i) present three positions of such a reconstruction). These 3D representations are used only for spatial visualization and refer to the procedure described in the last paragraph of Chp. 3.3.

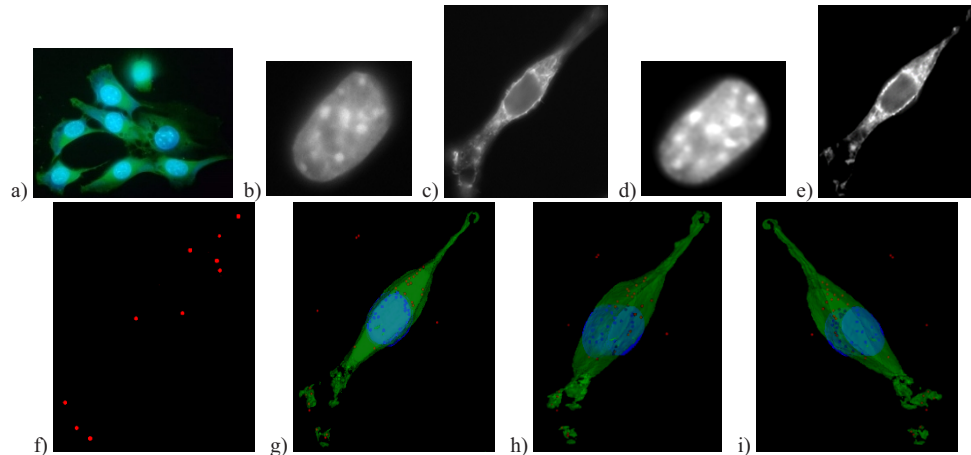


Fig. 8. a) Fluorescence image of a group of NIH3T3 cells (experimental colors through F4 filter); b) cross-section from F1-Z-stack; c) cross-section from F2-Z-stack; d) deconvolved image of b; e) deconvolved image of c; f) cross-section from WL-Z-stack with localized ZnO-NPs; g-i) movie frames obtained by combining all Z-stacks (digital colors).

4.3. Output parameters

ZnO-NPs densities at different extracellular NPs concentrations by cell regions (nucleus, shell 1, cytoplasm, shell 2) are presented in Fig. 9(a). It can be observed the followings: i/ very low particle density in the nuclei irrespective the extracellular NPs concentrations (blue bars in Fig. 9(a)), ii/ NPs density in cytoplasm proportional to extracellular concentration (green bars in Fig. 9(a)), iii/ NPs density in shell 1 proportional to extracellular concentration (yellow bars in Fig. 9(a)) excepting for 32 mg/mL. However, at 32 mg/mL, the particle density in shell 2 is significantly higher than for all other extracellular concentrations (orange bar in Fig. 9(a)).

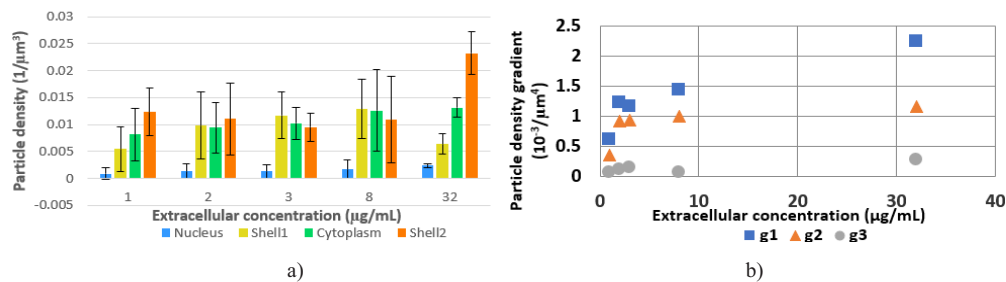


Fig. 9. a) Particle densities by cellular regions for different extracellular concentrations; b) NPs gradients (g1, g2, and g3) transverse to the layers adjacent to cell membrane.

Preferential accumulations of various categories of NPs in different types of cells were highlighted by complex biochemical methods and consequently specific NPs densities in different

cell regions were reported: inside the nucleus [52], around the nucleus, in the endoplasmic reticulum [30], or mainly located in the cytoplasm [53].

In the case of ZnO-NPs, their presence in the cytoplasm was already confirmed in different types of cells [54], but details about their more precise location are still difficult to specify. Sophisticated biochemical analysis indicated autophagosome accumulation of ZnO-NPs in PC₁₂ cells [55] and attributed the destruction of cells by ZnO-NPs to an accumulation of such toxic NPs in the bacterial membrane [56]. Our method allows to establish a quite detailed map of NPs over the regions defined herein by processing double labeled fluorescence images obtained through standard experimental procedures.

When inspecting the gradients of particle densities (Fig. 9(b)), it is worth noting that, in the immediate vicinity of the plasma membrane (between the first and the second layers, blue squares in Fig. 9(b)), the highest gradient of ZnO-NPs can be observed. This gradient decreases significantly between the second and third layer (Fig. 9(b), orange triangles), and diminishes to zero between the last ones (Fig. 9(b), grey circles). In all cases, the higher the extracellular NPs concentration, the higher the gradient. This means that there is an accumulation of NPs in the layers situated immediately below the membrane, while in the deeper layers, NPs distribution tends to a homogenous one.

The ANOVA test was run to compare the sets of particle densities on the four regions (each region with each other); it returned $F = 11.13959$, $F_{\text{crit}} = 3,23887$, $p\text{-value} = 0.00034$. Because $F > F_{\text{crit}}$ and $p < 0.001$, statistically significant differences among the particle densities by cellular regions are revealed.

The relative accumulation index (RAI) was used to assess the extent to which NPs exhibit preferential localization in a certain region (a RAI > 1 indicates preference). A chi-square test compares the measured number of ZnO-NPs in each region against the expected number of particles computed under the null hypothesis. One can observe that Shell 2 is the preferential localization region for ZnO-NPs in the case of extracellular concentrations of 1 $\mu\text{g/mL}$, 2 $\mu\text{g/mL}$ and 32 $\mu\text{g/mL}$ (Table 1) and cytoplasm for 8 $\mu\text{g/mL}$, because the following set of three criteria are simultaneously met [57]: i/ RAI is greater than 1, ii/ $p\text{-value} < 0.001$, and iii/ the region's own chi-squared accounts for more than 10% from cumulated chi-squared values of all regions. In these cases, the individual chi-squared values have substantial contributions to the total chi-squared (approx. 38%, 21%, 52% and 17% respectively). In the case of 3 $\mu\text{g/mL}$ extracellular concentration (Table 1) the three criteria above are not met. For all extracellular concentrations, the number of ZnO-NPs in nucleus region is the lowest. Concluding, based on this test, the null hypothesis is rejected for 1 $\mu\text{g/mL}$, 2 $\mu\text{g/mL}$, 8 $\mu\text{g/mL}$ and 32 $\mu\text{g/mL}$. These results are in line also with hyperspectral images (Figs. 6(c), 7).

Table 1. ZnO-NPs localization by regions as revealed by RAI and chi-squared values.

	RAI	chi-squared	RAI	chi-squared	RAI	chi-squared	RAI	chi-squared	RAI	chi-squared
Nucleus	0.10	12.72	0.13	21.52	0.15	12.37	0.21	23.51	0.20	31.06
Shell 1	0.80	0.44	1.25	1.04	1.16	0.47	1.36	3.39	0.53	6.81
Cytoplasm	1.23	0.85	1.15	0.91	1.09	0.35	1.40	5.63	1.14	0.84
Shell 2	1.69	8.74	1.43	6.26	1.14	0.98	1.16	1.01	1.89	42.25
	22.74		29.73		14.17		33.54		80.97	
p-value	< 0.001		< 0.001		< 0.01		< 0.001		< 0.001	
Extracellular concentration	1 ($\mu\text{g/mL}$)		2 ($\mu\text{g/mL}$)		3 ($\mu\text{g/mL}$)		8 ($\mu\text{g/mL}$)		32 ($\mu\text{g/mL}$)	

RAI was successfully used in the case of transmission electron microscopy (TEM) images to quantify the distribution of immunogold NPs within cells [57]. Although the layers analyzed by

TEM have the same thickness (100 nm) as in the case of CytoViva Z-stacks, the advantage of our method is that it can quickly and automatically analyze tens of such wafers, because samples do not need special individual preparation of each section as in TEM.

As concerns the axial distribution of ZnO-NPs along OZ axis (see Fig. 10), one can observe that there is no significant preference of ZnO-NPs localization along OZ, at least at this level of granulation.

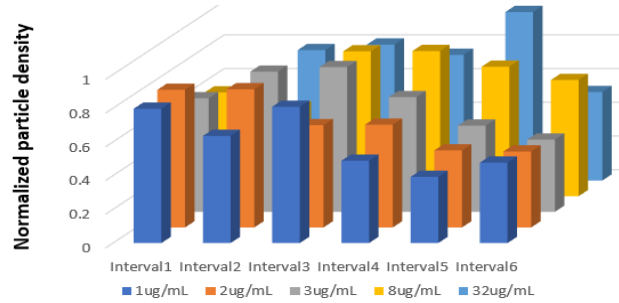


Fig. 10. Normalized particle density (mean values) along OZ axis for each extracellular concentration.

The particle density per whole cell and the flow density (as mean values over all cells) as a function of extracellular concentration are shown in Fig. 11(a) and (b) respectively. Despite the large standard deviations, a saturation effect is observable at higher extracellular ZnO-NPs concentrations.

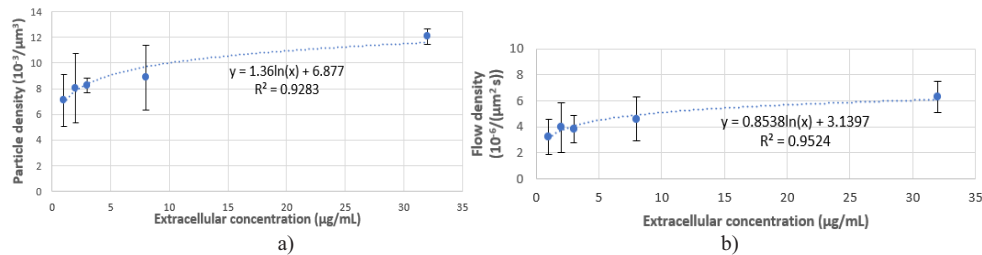


Fig. 11. The dependence on NPs extracellular concentration of a) particle density per whole cell, and b) flow density.

The ZnO-NPs uptake ratio is shown in Fig. 12 where the same saturating behavior at high ZnO-NPs extracellular concentration was observed.

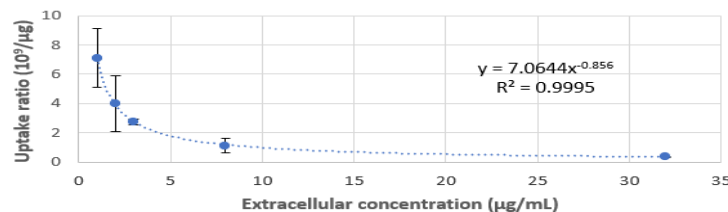


Fig. 12. The dependence of the uptake ratio on extracellular concentration.

In both Figs. 11 and 12, the fitting functions were formally used to evidence a sort of saturation behavior for the NPs uptake process without considering any explanatory biological mechanism.

Aiming to see if the number of NPs inside the cell and the cell geometry are linked, correlation coefficients comparing these parameters were computed. Strong positive correlation coefficients were found between the number of NPs inside the whole cell and the cell volume, and between NPs number and the cell lateral area (0.64 and 0.61 Pearson correlation coefficients, respectively). The bigger the cell, the more ZnO-NPs penetrate inside. For ZnO-NPs and NIH3T3 cells, our data indicated a moderate negative correlation between the number of nanoparticles inside the cell and the cell eccentricity (Pearson correlation coefficients -0.42). The higher the density of ZnO-NPs inside the cell, the lower the eccentricity (as cells lose their viability, *vide infra*, they become closer to a spherical shape, tending to zero eccentricity).

4.4. Viability assay

The viability assay results showed that at low extracellular NPs concentrations (up to 4 $\mu\text{g/mL}$), the cells keep their viability (Fig. 13). At higher extracellular concentrations (above 8 $\mu\text{g/mL}$) the cellular viability decreases abruptly as the NPs concentration increases. There are no differences in viability at ZnO-NPs concentrations higher than 8 $\mu\text{g/mL}$. These results agree with the behavior observed at high NPs extracellular concentration (Fig. 11(a)) and with the eccentricity dependence on NPs concentration (eccentricity tends to zero when NPs concentration is high, and dying cells become round).

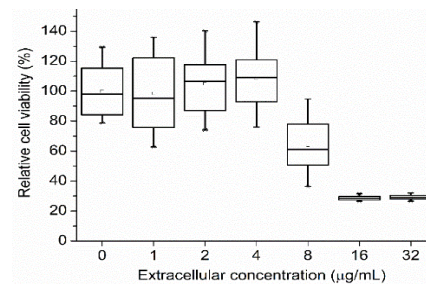


Fig. 13. The metabolic viability of NIH3T3 cells incubated for 24 h with different concentrations of ZnO-NPs.

5. Conclusions

We presented a method to improve the localization capabilities of joined eDFM, hyperspectral imaging, and Z-scan on double labeled fluorescent samples in CytoViva system; new techniques for cell mapping and counting unlabeled NPs in pre-defined cell regions were proposed and demonstrated. Differing from our previous work (Nanoscale 2022), here we used a more complex segmentation and NPs counting procedures using MATLAB scripts for data processing and quantitative evaluations of geometric characteristics and specific parameters as well: particle density, axial distribution, gradients in the vicinity of the cells' outer border, relative accumulation index, flow density through the cell lateral area, uptake ratio, and correlations.

Based on this improved computational method, some important features of the NPs uptake by the cells could be evidenced: intracellular NPs density increases with the extracellular concentration until reaching a sort of saturation; the highest density of NPs is in the immediate vicinity of the plasma membrane and tends to lower values in the cellular interior; the negative correlation of cell eccentricity with number of NPs inside cell was explained by the decrease of the cellular metabolic viability.

These are observed in the case of NIH3T3 cells and ZnO-NPs, but further developments include the using of other cell lines and various types of NPs. This approach offers the possibility to locate NPs more precisely in cells and consequently to better understand the mechanisms of

their influence on cellular processes. Moreover, it could allow to investigate the NPs distribution within regions at different moments, and therefore to build realistic models of their kinetics, thus contributing to understand the biological uptake mechanisms.

Funding. Unitatea Executiva pentru Finantarea Invatamantului Superior, a Cercetarii, Dezvoltarii si Inovarii (P_36_611, MySMIS code 107066).

Acknowledgments. AMP and RDN acknowledged the project UPB Proof of Concept. Hyperspectral and 3D imaging on CytoViva equipment was possible due to European Regional Development Fund through Competitiveness Operational Program 2014-2020, Priority axis 1, Project No. P_36_611, MySMIS code 107066, Innovative Technologies for Materials Quality Assurance in Health, Energy and Environmental—Center for Innovative Manufacturing Solutions of Smart Biomaterials and Biomedical Surfaces – INOVABIOMED.

Disclosures. The authors declare no conflicts of interest

Data availability. Data underlying the results presented in this paper are not publicly available at this time but may be obtained from the authors upon reasonable request.

References

1. D. Sawah, M. Sahloul, and F. Ciftci, "Nano-material utilization in stem cells for regenerative medicine," *Biomed. Eng.* **67**(6), 429–442 (2022).
2. K. T. Thurn, E. Brown, A. Wu, S. Vogt, B. Lai, J. Maser, T. Paunesku, and G. E. Woloschak, "Nanoparticles for Applications in Cellular Imaging," *Nanoscale Res. Lett.* **2**(9), 430–441 (2007).
3. R. Augustine, A. Hasana, R. Primavera, R. J. Wilson, A. S. Thakor, and B. D. Kevadiya, "Cellular uptake and retention of nanoparticles: Insights on particle properties and interaction with cellular components," *Mat. Today Comm.* **25**, 101692 (2020).
4. M. Faizan, S. Hayat, and J. Pichtel, "Effects of zinc oxide nanoparticles on crop plants: a perspective analysis," *Sustain. Agric. Rev.* **41**, 83–99 (2020).
5. M. Azahar Ali, K. Mondal, C. Singh, B. D. Malhotra, and A. Sharma, "Anti-epidermal growth factor receptor conjugated mesoporous zinc oxide nanofibers for breast cancer diagnostics," *Nanoscale* **7**(16), 7234–7245 (2015).
6. L. S. Reddy, M. M. Nisha, M. Joice, and P. N. Shilpa, "Antimicrobial activity of zinc oxide ZnO nanoparticle against *Klebsiella pneumoniae*," *Pharm Biol* **52**(11), 1388–1397 (2014).
7. Y. Hu, H.R. Zhang, L. Dong, M.R. Xu, L. Zhang, W.P. Ding, J.Q. Zhang, J. Lin, Y. J. Zhang, B.S. Qiu, P.F. Wei, and L.P. Wen, "Enhancing tumor chemotherapy and overcoming drug resistance through autophagy-mediated intracellular dissolution of zinc oxide nanoparticles," *Nanoscale* **11**(24), 11789–11807 (2019).
8. A. Czyżowska and A. Barbasz, "A review: zinc oxide nanoparticles – friends or enemies?" *Internat. J of Envir. Health Res.* **32**(4), 885–901 (2022).
9. C. Wang, X. Hu, Y. Gao, and Y. Ji, "ZnO nanoparticles treatment induces apoptosis by increasing intracellular ROS levels in LTP-a-2 cells," *Biomed. Res. Internat.* **2015**, 1–9 (2015).
10. M. Malatesta, "Transmission electron microscopy as a powerful tool to investigate the interaction of nanoparticles with subcellular structures," *Int. J. Mol. Sci.* **22**(23), 12789 (2021).
11. M.I. Rasel, S. Singh, T.D. Nguyen, I. O. Afara, and Y. Gu, "Impact of nanoparticle uptake on the biophysical properties of cell for biomedical engineering applications," *Sci. Rep.* **9**(1), 5859 (2019).
12. G. Pyrgiotakis, C. O. Blattmann, and P. Demokritou, "Real-time nanoparticle–cell interactions in physiological media by atomic force microscopy," *ACS Sustain Chem Eng* **2**(7), 1681–1690 (2014).
13. G. Zhou, B. Zhang, G. Tang, X. F. Yu, and M. Galluzzi, "Cells nanomechanics by atomic force microscopy: focus on interactions at nanoscale," *Adv. Phys: X* **6**(1), 1866668 (2021).
14. H. H. Chen, C. C. Chien, C. Petibois, C.-L. Wang, Y. S. Chu, S.-F. Lai, T.-E. Hua, Y.-Y. Chen, X. Cai, I. M. Kempson, Y. Hwu, and G. Margaritondo, "Quantitative analysis of nanoparticle internalization in mammalian cells by high resolution X-ray microscopy," *J Nanobiotech.* **9**(1), 14 (2011).
15. A. Foetisch, M. Filella, B. Watts, L. H. Vinot, and M. Bigalke, "Identification and characterisation of individual nanoplastics by scanning transmission X-ray microscopy (STXM)," *J. Hazardous Mat.* **426**, 127804 (2022).
16. Q. Li, F. Wang, J. Yang, and D. Liu, "Direct cytoplasm delivery of gold nanoparticles for real-time apoptosis detection," *Nano Res.* **13**(3), 853–860 (2020).
17. J. J. Rennick, A. P. R. Johnston, and R. G. Parton, "Key principles and methods for studying the endocytosis of biological and nanoparticle therapeutics," *Nat. Nanotechnol.* **16**(3), 266–276 (2021).
18. J. Vangindertael, R. Camacho, W. Sempels, H. Mizuno, P. Dedecker, and K. P. F. Janssen, "An introduction to optical super-resolution microscopy for the adventurous biologist," *Methods Appl. Fluoresc.* **6**(2), 022003 (2018).
19. A. Beghin, A. Kechkar, C. Butler, F. Levet, M. Cabillic, O. Rossier, G. Giannone, R. Galland, D. Choquet, and J. B. Sibarita, "Localization-based super-resolution imaging meets high-content screening," *Nat. Methods* **14**, 1184–1190 (2017).
20. Y. Li, C. Jing, L. Zhang, and Y. T. Long, "Resonance scattering particles as biological nanosensors in vitro and in vivo," *Chem. Soc.Rev.* **41**(2), 632–642 (2012).

21. M. Hu, C. Novo, A. Funston, H. Wang, H. Staleva, S. Zou, P. Mulvaney, Y. Xia, and G. V. Hartland, "Dark-field microscopy studies of single metal nanoparticles: understanding the factors that influence the linewidth of the localized surface plasmon resonance," *J. Mater. Chem.* **18**(17), 1949 (2008).
22. J. J. Evans, "An image-processing technique for measuring the dynamic movement of cell membranes," *Comput. In Biol. And Medicine* **38**(5), 545–554 (2008).
23. R. Emillie, B. Sharma, A.-I. Henry, L. D. Marks, and R. P. Van Duyne, "Single nanoparticle plasmonics," *Chem. Phys.* **51**(17), 4181–4184 (2012).
24. T. A. El-Brolosy, T. Abdallah, M. B. Mohamed, S. Abdallah, K. Easawi, S. Negm, and H. Talaat, "Shape and size dependence of the surface plasmon resonance of gold nanoparticles studied by Photoacoustic technique," *Eur. Phys. J. Special Topics* **153**(1), 361–364 (2008).
25. R. Lehner, I. Zanoni, A. Banuscher, A. L. Costa, and B. Rothen-Rutishauser, "Fate of engineered nanomaterials at the human epithelial lung tissue barrier in vitro after single and repeated exposures," *Front. Toxicol.* **4**, 918633 (2022).
26. P. Zamora-Perez, B. Pelaz, D. Tsoutsis, M. G. Soliman, W. J. Parak, and P. Rivera-Gil, "Hyperspectral-enhanced dark field analysis of individual and collective photo-responsive gold–copper sulfide nanoparticles," *Nanoscale* **13**(31), 13256–13272 (2021).
27. S.-F. Fobian, M. Petzer, M. Vetten, V. Steenkamp, M. Gulumian, and W. Cordier, "Mechanisms facilitating the uptake of carboxyl–polythene glycol-functionalized gold nanoparticles into multicellular spheroids," *J. Pharmacy and Pharmacology* **74**(9), 1282–1295 (2022).
28. G. A. Roth, M. del P Sosa Peña, N. M. Neu-Baker, S. Tahiliani, and S. A. Brenner, "Identification of metal oxide nanoparticles in histological samples by enhanced darkfield microscopy and hyperspectral mapping," *J. Visual. Experim.* **106**, e53317 (2015).
29. C. Grabinski, J. Schlager, and S. Hussain, "Hyperspectral microscopy for characterization of gold nanoparticles in biological media and cells for toxicity assessment," *Nanomat. Interf. in Biol.* **1025**, 167–178 (2013).
30. R. Fakhrullin, L. Nigamatzyanova, and G. Fakhrullin, "Dark-field/hyperspectral microscopy for detecting nanoscale particles in environmental nanotoxicology research," *Sci. Total Environ.* **772**, 145478 (2021).
31. F. Akhatova, A. Danilushkina, G. Kuku, M. Saricam, M. Culha, and R. Fakhrullin, "Simultaneous intracellular detection of plasmonic and non-plasmonic nanoparticles using dark-field hyperspectral microscopy," *Bull. of the Chem. Soc. of Japan* **91**(11), 1640–1645 (2018).
32. S. Lawrence, "Enhanced darkfield optical microscopy opens new nano-scale imaging possibilities," *Microsc. Today* **29**(1), 50–55 (2021).
33. P. Zhang, K. Kim, S. Lee, S. K. Chakkarapani, N. Fang, and S. H. Kang, "Augmented 3D super-resolution of fluorescence-free nanoparticles using enhanced dark-field illumination based on wavelength-modulation and a least-cubic algorithm," *Sci. Rep.* **6**(1), 32863 (2016).
34. I. A. Paun, B. S. Calin, C. C. Mustaciosu, M. Mihailescu, A. Moldovan, O. Crisan, A. Leca, and C. R. Luculescu, "3D superparamagnetic scaffolds for bone mineralization under static magnetic field stimulation," *Materials* **12**(17), 2834 (2019).
35. I. A. Paun, C. C. Mustaciosu, M. Mihailescu, B. S. Calin, and A. M. Sandu, "Magnetically-driven 2D cells organization on superparamagnetic micromagnets fabricated by laser direct writing," *Sci. Rep.* **10**(1), 16418 (2020).
36. L. C. Miclea, M. Mihailescu, N. Tarba, A.-M. Brezoiu, A. M. Sandu, R.-A. Mitran, D. Berger, C. Matei, M. G. Moisesescu, and T. Savopol, "Evaluation of intracellular distribution of folate functionalized silica nanoparticles using fluorescence and hyperspectral enhanced dark field microscopy," *Nanoscale* **14**(35), 12744–12756 (2022).
37. R. M. Zucker, J. Ortenzio, L. L. Degen, J. M. Lerner, and W. K. Boyes, "Biophysical comparison of four silver nanoparticles coatings using microscopy, hyperspectral imaging and flow cytometry," *PLoS One* **14**(7), e0219078 (2019).
38. D. L. Chi, E. Song, A. Gaudin, and W. M. Saltzman, "Improved threshold selection for the determination of volume of distribution of nanoparticles administered by convection-enhanced delivery," *Computer. Med. Imag. and Graph.* **62**, 34–40 (2017).
39. K. Hoshino, P. P. Joshi, G. Bhawe, K. V. Sokolov, and X. Zhang, "Use of colloidal quantum dots as a digitally switched swept light source for gold nanoparticle based hyperspectral microscopy," *Biomed. Opt. Express* **5**(5), 1610–1615 (2014).
40. D. Katoozi, A. H. A. Clayton, D. J. Moss, and J. W. M. Chon, "Uptake quantification of gold nanoparticles inside of cancer cells using high order image correlation spectroscopy," *Biomed. Opt. Express* **12**(1), 539–552 (2021).
41. A. P. Toropova, A. A. Toropov, A. Leszczynska, and J. Leszczynski, "Application of quasi-SMILES to the model of gold-nanoparticles uptake in A549 cells," *Comp. in Biol. and Medicine* **136**, 104720 (2021).
42. T. Popescu, C. O. Matei, I. D. Vlaicu, I. Tivig, A. C. Kuncser, M. Stefan, D. Ghica, L. C. Miclea, T. Savopol, D. C. Culita, and M. G. Moisesescu, "Influence of surfactant-tailored Mn-doped ZnO nanoparticles on ROS production and DNA damage induced in murine fibroblast cells," *Sci. Rep.* **10**(1), 18062 (2020).
43. J. A. Bartrop, T. C. Owen, A. H. Cory J, and G. Cory, "5-(3-carboxymethoxyphenyl)-2-(4,5-dimethylthiazolyl)-3-(4-sulfophenyl)tetrazolium, inner salt (MTS) and related analogs of 3-(4,5-dimethylthiazolyl)-2,5-diphenyltetrazolium bromide (MTT) reducing to purple water-soluble formazans As cell-viability indicators," *Bioorg. Med. Chem. Lett.* **1**(11), 611–614 (1991).
44. Cytoviva, "Hyperspectral Microscope User Manual," https://www.cytoviva.com/_files/ugd/338c3a_16c60aa74e0d4ee4b420f7ae6fb28ac5.pdf.

45. B. Tang, Z. Liu, X. Xiao, M. Nie, J. Chang, W. Jiang, X. Li, and C. Zheng, "Spectral-spatial hyperspectral classification based on multi-center SAM and MRF," *Opt. Rev.* **22**(6), 911–918 (2015).
46. Cytoviva 3-D, https://www.cytoviva.com/_files/ugd/338c3a_8f8e9baed3f84cf8978c86c18075b135.pdf.
47. Bwconvhull, "Generate convex hull image from binary image," MathWorks. <https://www.mathworks.com/help/images/ref/bwconvhull.html>.
48. alphaShape, "Polygons and polyhedra from points in 2-D and 3-D," MathWorks. <https://www.mathworks.com/help/matlab/ref/alphashape.html>.
49. A. Gelman, "Analysis of variance? Why it is more important than ever?" *The Annals of Statistics* **33**, 1–53 (2005).
50. M. Mortimer, A. Gogos, N. Bartolome, A. Kahru, T. D. Bucheli, and V. I. Slaveykova, "Potential of hyperspectral imaging microscopy for semi-quantitative analysis of nanoparticle uptake by protozoa," *Environ. Sci. Technol.* **48**(15), 8760–8767 (2014).
51. A. S. Kashani, A. Piekny, and M. Packirisamy, "Using intracellular plasmonics to characterize nanomorphology in human cells," *Microsyst. Nanoeng.* **6**(1), 110 (2020).
52. S. Huo, S. Jin, X. Ma, X. Xue, K. Yang, A. Kumar, P. C. Wang, J. Zhang, Z. Hu, and X. J. Liang, "Ultrasmall gold nanoparticles as carriers for nucleus-based gene therapy due to size-dependent nuclear entry," *ACS Nano* **8**(6), 5852–5862 (2014).
53. K. Song, P. Xu, Y. Meng, F. Geng, J. Li, Z. Li, J. Xing, J. Chen, and B. Kong, "Smart gold nanoparticles enhance killing effect on cancer cells," *Int J Oncol* **42**(2), 597–608 (2013).
54. .K.S. Siddiqi, A. U Rahman, A. Tajuddin, and Husen, "Properties of zinc oxide nanoparticles and their activity against microbes," *Nanoscale Res. Lett.* **13**(1), 141 (2018).
55. Z. Liu, X. Lv, L. Xu, X. Liu, X. Zhu, E. Song, and Y. Song, "Zinc oxide nanoparticles effectively regulate autophagic cell death by activating autophagosome formation and interfering with their maturation," *Part. Fibre Toxicol* **17**(1), 46 (2020).
56. B. Ahmed, F. Ameen, A. Rizvi, K. Ali, H. Sonbol, A. Zaidi, M. S. Khan, and J. Musarrat, "Destruction of cell topography, morphology, membrane, inhibition of respiration, biofilm formation, and bioactive molecule production by nanoparticles of Ag, ZnO, CuO, TiO₂, and Al₂O₃ toward beneficial soil bacteria," *ACS Omega* **5**(14), 7861–7876 (2020).
57. M. M. Terry, C. Muhlfeld, D. Vanhecke, and M. Ochs, "A review of recent methods for efficiently quantifying immunogold and other nanoparticles using TEM sections through cells, tissues and organs," *Annals of Anat. – Anat. Anzeiger* **191**(2), 153–170 (2009).